



Half-precessional cycle of thermocline temperature in the western equatorial Pacific and its bihemispheric dynamics

Zhimin Jian^{a,1}, Yue Wang^a, Haowen Dang^a, David W. Lea^b, Zhengyu Liu^c, Haiyan Jin^a, and Yaqian Yin^a

^aState Key Laboratory of Marine Geology, Tongji University, 200092 Shanghai, China; ^bDepartment of Earth Science, University of California, Santa Barbara, CA 93106; and ^cDepartment of Geography, Ohio State University, Columbus, OH 43210

Edited by Thomas M. Marchitto, University of Colorado, and accepted by Editorial Board Member Jean Jouzel February 17, 2020 (received for review September 8, 2019)

The El Niño–Southern Oscillation (ENSO), which is tightly coupled to the equatorial thermocline in the Pacific, is the dominant source of interannual climate variability, but its long-term evolution in response to climate change remains highly uncertain. This study uses Mg/Ca in planktonic foraminiferal shells to reconstruct sea surface and thermocline water temperatures (SST and TWT) for the past 142 ky in a western equatorial Pacific (WEP) core MD01-2386. Unlike the dominant 100-ky glacial–interglacial cycle recorded by SST and $\delta^{18}\text{O}$, which echoes the pattern seen in other WEP sites, the upper ocean thermal gradient shows a clear half-precessional (9.4 ky or 12.7 ky) cycle as indicated by the reconstructed and simulated temperature (ΔT) and $\delta^{18}\text{O}$ differences between the surface and thermocline waters. This phenomenon is attributed to the interplay of subtropical-to-tropical thermocline anomalies forced by the antiphased meridional insolation gradients in the two hemispheres at the precessional band. In particular, the TWT shows greater variability than SST, and dominates the ΔT changes which couple with the west–east SST difference in the equatorial Pacific at the half-precessional band, implying a decisive role of the tropical thermocline in orbital-scale climate change.

thermocline temperature | half-precession | western equatorial Pacific | meridional gradient

Present-day climate is significantly affected by the tropical Pacific (1). The western Pacific warm pool, which has a permanent sea surface temperature (SST) of $>28^\circ\text{C}$, is the largest reservoir of warm upper water on Earth and hence a heat engine for global climate. Furthermore, thermocline temperature in the western equatorial Pacific (WEP) contributes significantly to the maintenance of the equatorial SST climatology and acts as a precursor of El Niño–Southern Oscillation (ENSO) variability through the eastward propagation of subsurface temperature anomalies (2, 3). Paleoceanographic records from the equatorial Pacific Ocean provide insight into ENSO behavior when global boundary conditions—ocean and atmosphere circulations, sea level and ice volume, atmospheric greenhouse gas concentration, and albedo—were different from today, and thus help in the projection of trends or variance of ENSO in response to climate change. The ENSO cycle is known to be a feature of Earth's climate in the geological past (4, 5), and its signal should be more prominent in the thermocline response, as in modern climate (6). However, a lack of tropical thermocline water temperature (TWT) records with high temporal resolution has limited our understanding of how ENSO responds to orbital changes (7, 8). Here we examine thermocline temperature evolution in the WEP over the past 142 ky to investigate long-term ENSO-like changes and three-dimensional ocean dynamics.

We use deep-sea sediment samples from core MD01-2386, which was collected from the WEP during the R/V *Marion Dufresne* 122 cruise in 2001 (Fig. 1; $01^\circ07.80'\text{N}$, $129^\circ47.56'\text{E}$; 2,816 m water depth), for reconstructing records of SST and TWT (*SI Appendix, Table S1*) based on the Mg/Ca ratios of surface-dwelling *Globigerinoides ruber sensu stricto* and thermocline-

dwelling *Pulleniatina obliquiloculata* planktonic foraminiferal shells, respectively. About 30 *G. ruber* and 20 *P. obliquiloculata* shells were picked from each sample of the upper 2,089 cm in the core, with an average sample interval of 2 cm (1,037 *G. ruber* samples and 887 *P. obliquiloculata* samples). Foraminiferal shells were pretreated following the procedure described by Lea et al. (16). Trace elements including Mg/Ca were determined in *G. ruber* samples from the upper 400 cm by Element2 inductively coupled plasma mass spectrometry (ICP-MS) at the Department of Earth Science, University of California, Santa Barbara, following the procedure in Lea et al. (17); the remaining samples were analyzed at the State Key Laboratory of Marine Geology, Tongji University, China, with an instrumental precision of 1.1% (1 SD). We use the species-specific Mg/Ca SST calibration of *G. ruber* developed in the study area (18). For TWT, the published calibrations of *P. obliquiloculata* Mg/Ca and temperature (18–21) have similar exponential constants (~ 0.09), which would result in comparable trends and amplitudes of TWT estimates. In order to better compare with previous studies, we apply the equation of Anand et al. (19) to calculate TWT. The error of TWT reconstruction, introduced by the Mg/Ca measurements of 87 replicates for *P. obliquiloculata* and Mg/Ca temperature calibrations (22), is estimated at $\pm 1.1^\circ\text{C}$.

Significance

The precessional insolation plays a critical role in modulating the low-latitude oceanographic changes through ENSO-like dynamics. While previous studies focused on the precessional insolation-induced low-latitude surface water changes, our well-dated, centennial-resolution proxy data and numerical simulation reveal the half-precession cycle of thermocline water temperature (TWT) in the western equatorial Pacific that directly linked to ENSO-like zonal temperature seesaw over the equatorial Pacific. These half-precessional TWT changes are proposed to originate from the interplay of subtropical-to-tropical thermocline anomalies forced by the antiphased meridional insolation gradients in the two hemispheres at the precessional band. This work illustrates that the tropical thermocline water could bridge the meridional climatic processes and the east–west ENSO-like dynamics at orbital timescales.

Author contributions: Z.J. designed research; Z.J., H.D., D.W.L., H.J., and Y.Y. performed experiment; Y.W. and Z.L. analyzed data; and Z.J., Y.W., H.D., and D.W.L. wrote the paper.

The authors declare no competing interest.

This article is a PNAS Direct Submission. T.M.M. is a guest editor invited by the Editorial Board.

Published under the PNAS license.

¹To whom correspondence may be addressed. Email: jian@tongji.edu.cn.

This article contains supporting information online at <https://www.pnas.org/lookup/suppl/doi:10.1073/pnas.1915510117/-DCSupplemental>.

First published March 16, 2020.

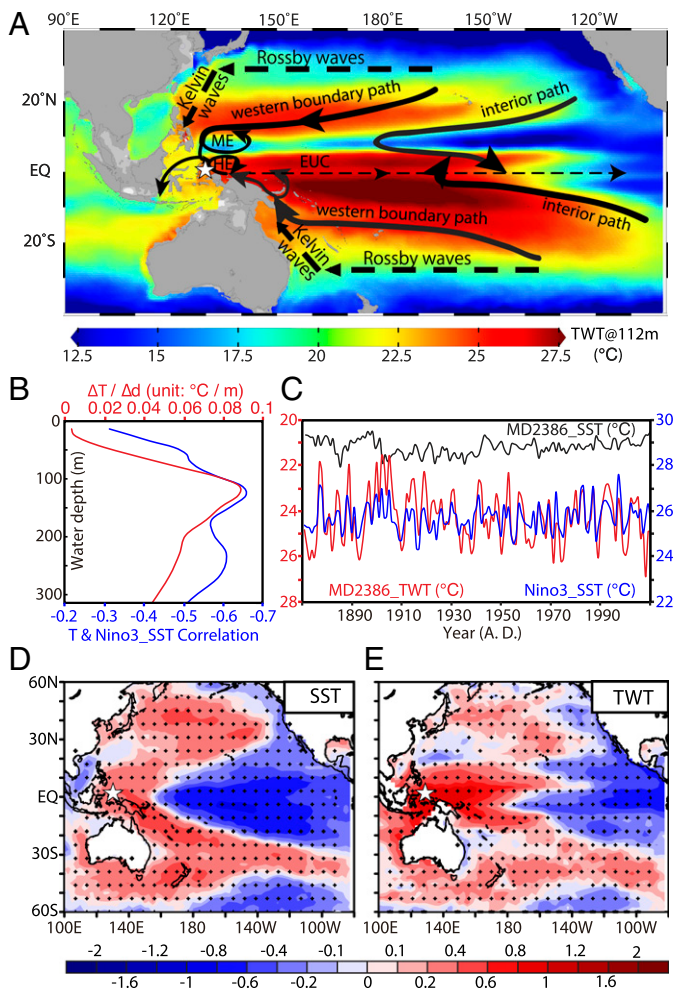


Fig. 1. Modern features of the thermocline water at site MD01-2386 based on the annual mean SODA reanalysis dataset over the years from 1871 to 2010 (9). (A) Core location (white star) and the tropical Pacific temperature at 112 m water depth—the tenth vertical layer of the SODA dataset—here denoted as TWT. For the STC, the black solid arrows indicate its western boundary and interior paths (10–12), whereas the black dashed arrows indicate its oceanic wave pathways (13–15). EUC, ME, and HE denote the Equatorial Undercurrent, Mindanao Eddy, and Halmahera Eddy, respectively. (B) For the SODA ocean temperature (T) at the location of MD01-2386 (01°07.80'N, 129°47.56'E), its vertical lapse rate (red line) and correlation with Nino3_SST (blue line) both reach maxima near the 120-m water depth. (C) MD2386_SST (black line) is highly correlated ($R = -0.66$) to MD2386_TWT (red line) but less correlated ($R = -0.14$) to MD2386_SST (black line), where “MD2386_” stands for regional averaged values of the nearest $0.5^\circ \times 0.5^\circ$ grid. *D* and *E* show spatial correlation coefficients of annual mean SST and TWT relative to the MD01-2386_TWT (red line in *C*). Dotted regions in *D* and *E* are significant at the 99% confidence level.

The age model of this core is established by 17 radiocarbon dates (Fig. 2 and *SI Appendix*, Table S2) of *G. ruber* (measured at Leibniz Laboratory, Kiel University, Germany) for the upper 980 cm of the core, as well as the correlations of planktonic *G. ruber* and benthic *Cibicides wuellerstorfi* $\delta^{18}\text{O}$ curves with the benthic $\delta^{18}\text{O}$ stack LR04 (24) (*SI Appendix*, Fig. S1). Radiocarbon dates are converted to calendar ages by program CALIB 7.1, and the depth–age relationship is established by applying the Bayesian statistical methodology of Bacon (25) (*SI Appendix*, Fig. S2). The stable isotopic analysis of *G. ruber* (1,226 samples, 2-cm interval), *P. obliquiloculata* (1,224 samples, 2-cm interval), and *C. wuellerstorfi* (410 samples, 2-cm interval from 0 cm to 600 cm and from 1,684 cm to 1,984 cm) were carried out using a

Finnigan MAT253 mass spectrometer at the State Key Laboratory of Marine Geology, Tongji University. Thus, the average time resolution of samples is ~ 120 y but with a higher resolution of ~ 60 y for the upper 980 cm in the core.

Half-Precessional Cycle in the Upper Thermal Structure. The SST reconstructed from core MD01-2386 varies between 24.4 °C and 29.3 °C, while the TWT fluctuates between 15.5 °C and 26.9 °C over the past 142 ky (Fig. 2). The Mg/Ca-derived SST and TWT averaged 27.5 ± 0.5 °C and 22.7 ± 0.7 °C (all errors quoted are 1 SD) during the Late Holocene (0 ka BP to 4 ka BP), respectively, close to the observed modern annual mean SST of 28.8 °C and TWT of 24.2 °C, as defined by the temperature at a depth of 112 m—the tenth vertical layer of the Simple Ocean Data Assimilation (SODA) dataset (9), and also the habitat depth of *P. obliquiloculata* [between 100 m and 150 m water depth (upper thermocline) (18, 26)] at this site. SST averaged 25.8 ± 0.6 °C across marine isotope stages (MISs) 2 to 4, and 28.4 ± 0.5 °C during MIS 5e, while the TWT averaged 21.2 ± 1.2 °C across MISs 2 to 4, and 23.5 ± 1.8 °C during MIS 5e. SST and TWT average 25.6 ± 0.5 °C and 21.5 ± 1.2 °C during the Last Glacial

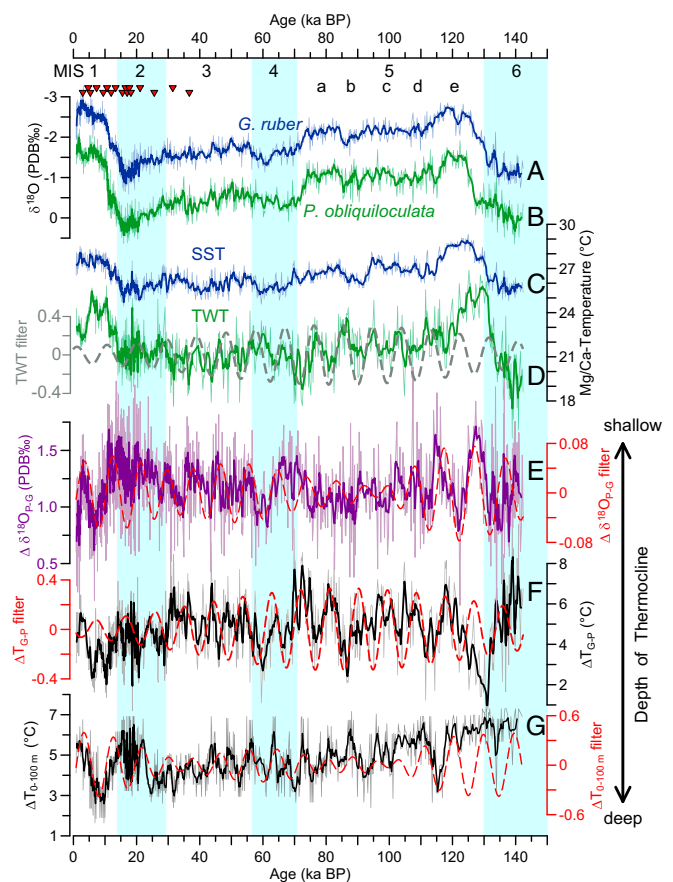


Fig. 2. Comparison of (A) *G. ruber* $\delta^{18}\text{O}$, (B) *P. obliquiloculata* $\delta^{18}\text{O}$, (C) SST (based on *G. ruber* Mg/Ca), and (D) TWT (based on *P. obliquiloculata* Mg/Ca), (E) $\delta^{18}\text{O}$ difference between *P. obliquiloculata* and *G. ruber* ($\Delta\delta^{18}\text{O}_{\text{P-G}}$), (F) temperature difference between SST and TWT ($\Delta T_{\text{G-P}}$), and (G) differences between the surface (0 m) and subsurface (100 m) temperatures ($\Delta T_{0-100\text{m}}$) estimated by the transfer function of SIMMAX28 (23). All bold curves are five-point moving average filters. Gray dashed line in *D* and red dashed lines in *E–G* denote the Gaussian band-pass filters (center frequency = 0.109 ky^{-1}) of TWT and $\Delta T_{\text{G-P}}$ (bandwidth = 0.005), and $\Delta\delta^{18}\text{O}_{\text{P-G}}$ and $\Delta T_{0-100\text{m}}$ (bandwidth = 0.015). MIS 1 to ~ 6 at the top indicates marine isotopic stages, while red triangles denote the accelerator mass spectrometry (AMS) ^{14}C age determinations.

Maximum (19 ka BP to 23 ka BP) and thus are lower than the Late Holocene mean by 1.9 ± 0.5 °C and 1.2 ± 0.9 °C, respectively.

The Mg/Ca reconstructed TWT (SD 1.68 °C) is more variable than the SST (SD 0.91 °C) (Fig. 2 C and D), as is also the case for modern observed TWT and SST (Fig. 1C; with SD of 1.14 °C and 0.34 °C, respectively). Especially, the millennial- to centennial-scale variability of the TWT exceeds the estimated error, suggesting greater short-term variability. The millennial-scale variability of TWT during the last glacial interval (SI Appendix, Fig. S3) displays behavior similar to Antarctic air temperature and atmospheric CO₂ (27, 28), implying a greenhouse gas forcing on tropical TWT variability and a potential climate link between the tropical Pacific and Southern Ocean, possibly via ocean tunnel connections (29, 30). Over Termination I, both SST and TWT display a clear mid-Termination plateau centered at ~12.5 ka BP (13.2 ka BP to 11.8 ka BP). A similar plateau has been identified in atmospheric CO₂ records and other tropical SST records (22, 31–33).

A five-point moving average filter was applied to all SST and TWT (1-σ range of variability is ±0.4 °C for SST and ±1.0 °C for TWT; Fig. 2). Generally, SST changes in parallel with the δ¹⁸O of *G. ruber*, displaying a typical 100-ky glacial–interglacial cycle with a peak-to-peak amplitude of 3 °C to 5 °C, consistent with previous studies (16). The TWT also exhibits a clear glacial–

interglacial cycle, but with a larger peak-to-peak amplitude of 5 °C to 8 °C, which is consistent with a newly published *P. obliquolucata* Mg/Ca TWT record of the last 110 ky (ref. 34 and SI Appendix, Fig. S4) from site GeoB17419-1 near site MD01-2386, indicating that TWT is more sensitive to orbital-scale climate change. After removing glacial–interglacial trends, the spectrum of SST is dominated by a strong precessional (22.8 ky) signal (Fig. 3A), similar to that at site MD05-2930 in the Gulf of Papua (37). Interestingly, an obvious half-precessional cycle (9.4 ky) (38) can be identified, even by naked eye, from the difference between SST and TWT (ΔT_{G-P}, denoting the upper water thermal gradient) over the past 142 ky (Fig. 2F), and is dominant in the spectrum of TWT and ΔT_{G-P} (Fig. 3B and C). The obliquity cycle is relatively weak in TWT and ΔT_{G-P} at site MD01-2386 and in TWT at site MD05-2930 (near 10°S) (37), slightly different from the dominant obliquity cycle in TWT record at site GeoB17419-1 north off Papua New Guinea near 2°S (34).

Mg/Ca ratios of sedimentary planktonic foraminifera are affected by the deep-water dissolution effect (21, 39, 40). Foraminifera shells from core MD01-2386 (2,816 m) were deposited in undersaturated bottom waters and likely experienced partial dissolution (see discussion in Methods). But, during the last two terminations, when the Mg/Ca temperatures change the most significantly (SI Appendix, Fig. S4), the planktonic foraminiferal fragmentation—the best indicator of dissolution (41)—remains

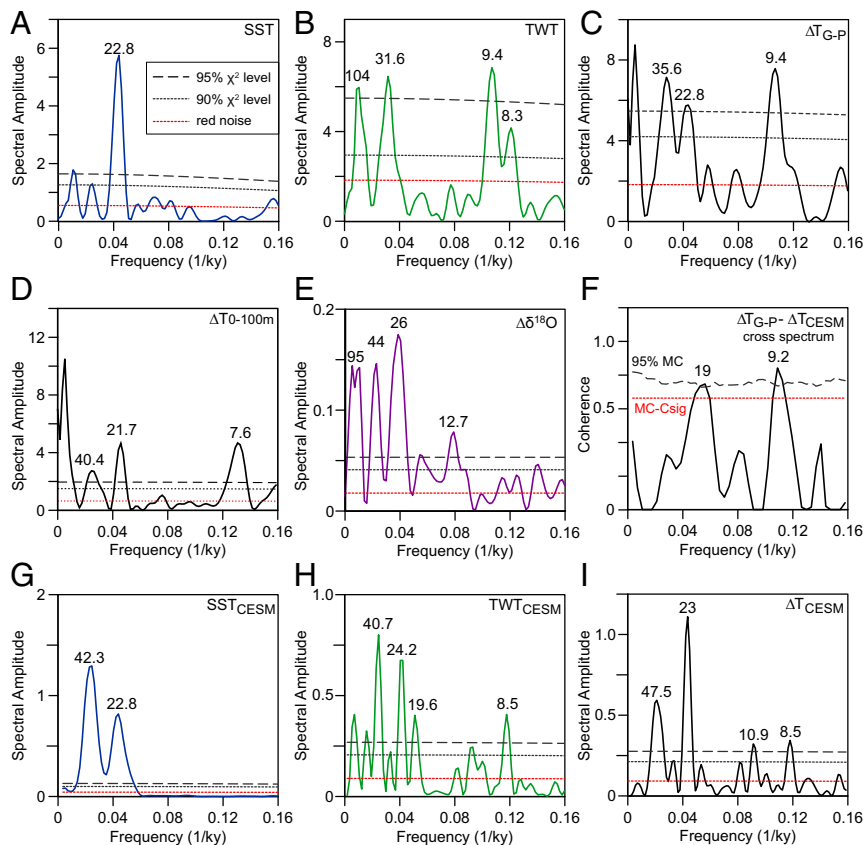


Fig. 3. Spectral amplitudes for the (A) SST, (B) TWT, and (C) ΔT_{G-P} records from core MD01-2386 are compared with those of the CESM modeled (G) SST_{CESM}, (H) TWT_{CESM}, and (I) ΔT_{CESM} at the same location. Also shown are spectral amplitudes of the (D) ΔT_{0-100m} and (E) Δδ¹⁸O_{P-G} from core MD01-2386, and (F) the cross-spectrum between ΔT_{G-P} and ΔT_{CESM}. Note that, before spectral analysis, glacial–interglacial changes of the Mg/Ca SST and TWT have been removed by a method of quintic polynomial fitting for a better comparison with the CESM simulation. The spectral analyses are performed by Redfit38 with Hanning (in A–E) or rectangular (in G–I) windows (oversample, 4; segment, 1) (35), and the cross-spectrum analysis is performed by Redfit-X with Hanning window (oversample, 4; segment, 3; MC, Monte Carlo; MC-Csig, Monte Carlo significant confidence) (36). Numbers above the spectrum curves in A–I denote those dominant periods (unit: kiloyears) exceeding the 95% confidence level, that is, 23- to 19-ky periods for precession and 12.7- to 8.5-ky periods for half-precession.

roughly constant. Although the fragmentation suggests relatively intensified deep-water dissolution during MISs 2 to 5d (*SI Appendix*, Fig. S4), its spectrum exhibits no significant peak at the precessional and half-precessional periods (*SI Appendix*, Fig. S5). Therefore, while it is possible that some of the TWT variability is due to dissolution, the main features, such as the half-precessional cycle, do not appear related to dissolution.

The half-precession variability of the reconstructed ΔT_{G-P} changes is confirmed by the temperature difference (ΔT) between the water depths of 0 m and 100 m (ΔT_{0-100m} ; Figs. 2*G* and 3*D*) reconstructed from the transfer function of planktonic foraminiferal census data (23). Both the ΔT_{G-P} and ΔT_{0-100m} show roughly the same range of variation ($\sim 6^\circ\text{C}$) and clear half-precessional cycles, and match well with each other except for the interval of 125 ka BP to 135 ka BP (Fig. 2*F* and *G*). The half-precessional variability is further confirmed in a transient sensitivity experiment in the Community Earth System Model 1.0.4 (CESM) under the orbital forcing since 300 ka and other boundary conditions in AD 1950 (called experiment CESM_{transient}). In this experiment, the model was integrated for 3,000 model years with the 100-fold accelerated orbital insolation forcing of the past 300 ky (detailed in *Methods*).

The modeled ΔT at site MD01-2386 (called ΔT_{CESM} ; *SI Appendix*, Fig. S7) shows a prominent half-precessional change that is statistically significant at 95% level (Fig. 3*I*), although the orbital insolation forcing only consists of eccentricity, obliquity, and precession (without a half-precession component). Despite the smaller variance in TWT and SST in the model (called TWT_{CESM} and SST_{CESM}), which results partly from the absence of other driving factors (i.e., ice sheet, sea level, and atmospheric greenhouse gases), the TWT_{CESM} also exhibits a larger magnitude of variation than the SST_{CESM} (with SDs of 0.39 °C and 0.22 °C, respectively; *SI Appendix*, Fig. S7), and the simulated vertical temperature difference ΔT_{CESM} is generally comparable to the proxy-reconstructed ΔT_{G-P} , notably, in periods and phase. This consistency in period and phase can be further seen in the cross-spectrum between ΔT_{G-P} and ΔT_{CESM} , which shows significant coherence in the half-precessional band (9.2 ky) at the 95% confidence level (Fig. 3*F*). The robustness of this half-precessional cycle in the WEP TWT seems to be also confirmed in the same type of transient experiment but in another independent air–sea coupled model (called Community Climate System Model version 3) (detailed in *SI Appendix*). This robust model–data consistency suggests that some features of the ΔT record from the WEP, and, in particular, its half-precessional cycle, could be forced by orbital insolation.

The difference between the oxygen isotope composition of thermocline-dwelling species *P. obliquiloculata* and surface-dwelling species *G. ruber* ($\Delta\delta^{18}\text{O}_{P-G}$; Fig. 2*E*) is widely used to indicate changes in the depth of the thermocline, with larger values representing a shallower thermocline (42, 43). Whereas the $\delta^{18}\text{O}$ curves of *P. obliquiloculata* and *G. ruber* display a typical glacial–interglacial cycle of 100 ky, the dominant period for the $\Delta\delta^{18}\text{O}_{P-G}$ is precession and half-precession (12.7 ky; Fig. 3*E*). The $\Delta\delta^{18}\text{O}_{P-G}$ is correlated to the ΔT_{G-P} with a cross-spectrum coherence of 0.85 at the 95% confidence level in the half-precessional band. The half-precession periods (12.7 and 9.4 ky) in this study (Fig. 3) are almost exactly half-periods of the two precessional periods (23 and 19 ky) (38, 44), but the periods are slightly different for TWT and ΔT_{G-P} (9.4 \pm 0.4 ky) and for $\Delta\delta^{18}\text{O}_{P-G}$ (12.7 \pm 0.6 ky) at the 95% confidence level (Fig. 3). A similar half-precessional period (12.0 ky) is also significant in the primary production index of coccolith at site MD01-2386 (*SI Appendix*, Fig. S4), indicating a nontrivial linkage between thermocline dynamics and phytoplankton productivity. The half-precessional cycle has been found in other records from equatorial regions (45–47), but our results indicate the existence of

half-precession cycle in proxies for the upper thermal gradient in the WEP, which is directly linked to ENSO. Our numerical study also provides modeling support of the half-precessional response in the WEP thermocline.

Equator–Subtropical Insolation Gradient Forcing from Two Hemispheres.

The TWT in the WEP is largely maintained by the thermocline waters subducted from the subtropical Pacific in both hemispheres in late local winter; these waters are transmitted to the WEP in the Subtropical–Tropical Cell (STC) through thermocline ventilation in the low-latitude western boundary pathway and oceanic Rossby and Kelvin waves (Fig. 1*A* and refs. 2, 10–12, 14 and 15, and 48–50). These mechanisms influencing modern TWT at the WEP should have also played an important role in the geological past. Because site MD01-2386 is located in the WEP and right at the crossroads of the western boundary pathways from both hemispheres (Fig. 1*A*), we hypothesize that the TWT at this site can be determined by the equatorward subsurface temperature anomalies transported by the STCs from both hemispheres.

The CESM_{transient} simulation shows that the precessional forced TWT changes at site MD01-2386 are alternatively controlled by the contrasting thermocline temperature anomalies from the North and South Pacific (Fig. 4*A* and *B*), indicating an interhemispheric interplay of the STCs from both hemispheres. For example, in boreal summer at precessional minimum, thermocline temperature is warmer (colder) in the subtropical North (South) Pacific (Fig. 4*A*) when Earth is closer to (farther away from) the sun in the Northern (Southern) Hemisphere, and is reversed at precessional maximum (Fig. 4*B*) (all of the signs are opposite in boreal winter; Fig. 4*C* and *D*). The thermocline temperature anomaly is then transported into the WEP through the STC, especially in the low-latitude western boundary current (10, 48, 50–52). Therefore, the equatorial thermocline temperature is determined by the contrasting thermocline temperatures and, in turn, insolation in the two hemispheres (53).

The similarity between ΔT_{G-P} and ΔT_{CESM} (Fig. 4*E*), as proved by cross-spectrum coherences of 0.78 at 19 ky and 0.88 at 9.2 ky (Fig. 3*F*), suggests that the half-precessional signal in the WEP thermocline water may be a “footprint” of the STCs from two hemispheres during different “seasons” in the precessional cycle. Indeed, the dynamic mechanism discussed above suggests that this signal should be the strongest in the western part of the equatorial thermocline, where the equatorward convergence is the strongest. This spatial structure of the half-precessional signal is confirmed by the tongue-shaped distribution of positive regression coefficient values in the ocean temperature field, both at the thermocline depth plane (Fig. 5*D*) and along the equatorial profile (Fig. 5*E*).

We further propose a conceptual model of theoretical ΔT forced by precessional insolation changes between the equator and subtropics of two hemispheres (Fig. 4*F* and *G*; detailed in *Methods* and *SI Appendix*, Fig. S8). Results from the CESM_{transient} experiment (*SI Appendix*, Fig. S10) show that the November meridional insolation gradient between 0°N and 30°N and the May insolation gradient between 0°N and 30°S can be taken as the original forcing of the subducted temperature anomaly in the North and South Pacific, respectively. The envelope curves of the two insolation gradients seem to be coincident with the half-precessional fluctuations of ΔT_{G-P} (Fig. 4*F* and *G*). Two minima or maxima of the envelope curves during each precession cycle [so-called “clipped precession” (45)], also shown in *SI Appendix*, Fig. S8*B*] may generate a signal of half-precessional period in the theoretical ΔT (Fig. 4*F*).

Except for Termination II, the half-precessional change of theoretical ΔT generally matches well with the five-point moving averaged ΔT_{G-P} at site MD01-2386 over the past 142 ky (Fig. 4*G*), with a cross-spectrum correlation of >0.50 at the 95% confidence level, supporting the hypothesis that the upper water thermal structure in the WEP is forced by the meridional

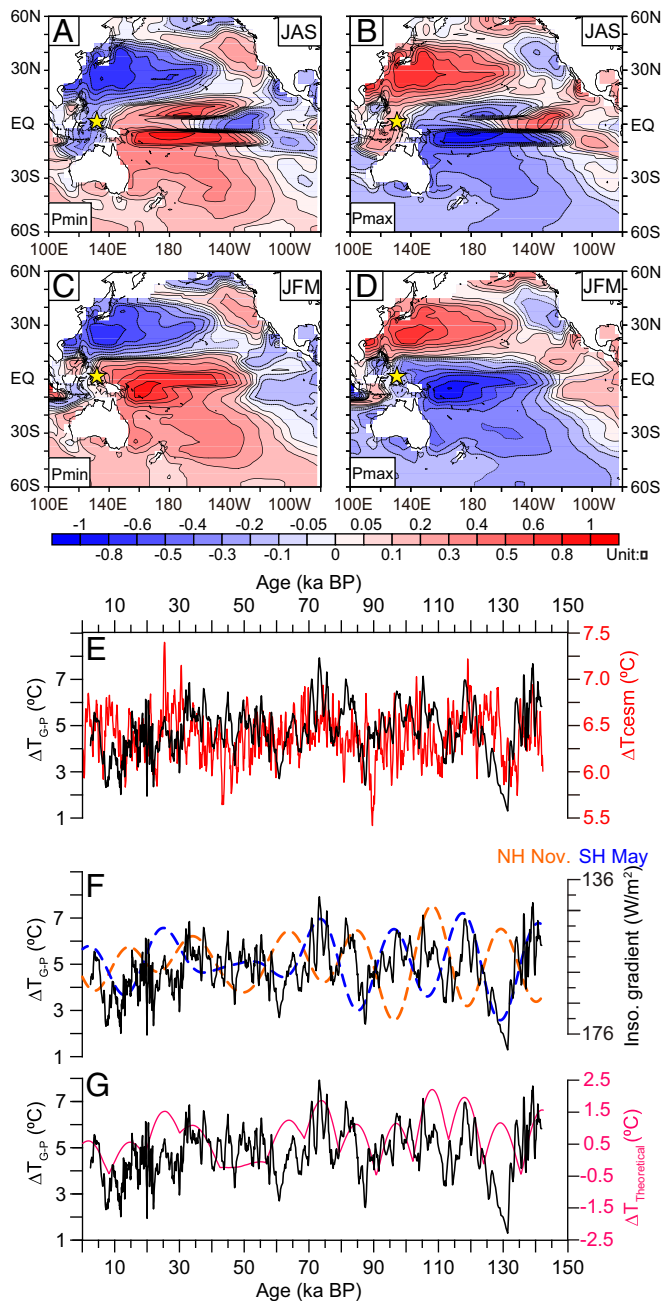


Fig. 4. A and B are composite difference of July–September (JAS; boreal summer) TWT relative to climatological mean from the CESM simulation during precessional (A) minimum and (B) maximum. C and D are composite difference of January–March (JFM; boreal winter) TWT relative to climatological mean during precessional (C) minimum and (D) maximum. Core location of MD01-2386 is shown as the yellow stars in A–D. (E) Five-point smoothed ΔT_{G-P} of core MD01-2386 is compared with that of the ΔT_{CESM} . (F) ΔT_{G-P} is compared with meridional insolation gradients between 0°N and 30°N during November (brown dashed line) and between 0°N and 30°S during May (blue dashed line). (G) The theoretical ΔT from a simplified conceptual model (detailed in *Methods*) is compared with ΔT_{G-P} .

equator-to-subtropical gradients of insolation or temperature in both hemispheres. For each precessional cycle, the ΔT_{G-P} at the WEP will show two peaks, due to the interplay of the STCs in both hemispheres (Fig. 4F), and may be closely related to the insolation-driven meridional migration of the Intertropical Convergence Zone (ITCZ) (11, 13, 54). Although a previous study

found no relationship between equatorial insolation and half-precession (55), subtropical forcing is hypothesized to generate a significant temperature response in the equatorial thermocline for forcing periods longer than decades (48), such as orbital-scale change in the Middle Pleistocene (56).

Role of Thermocline in the Orbital-Scale ENSO-like Changes. It has been proposed that changes in tropical Pacific SST parallel atmospheric CO₂ concentration and precede the $\delta^{18}O$ changes during glacial terminations (16, 17, 57), supporting greenhouse gas forcing on tropical climate (30, 58). In this study, the SST,

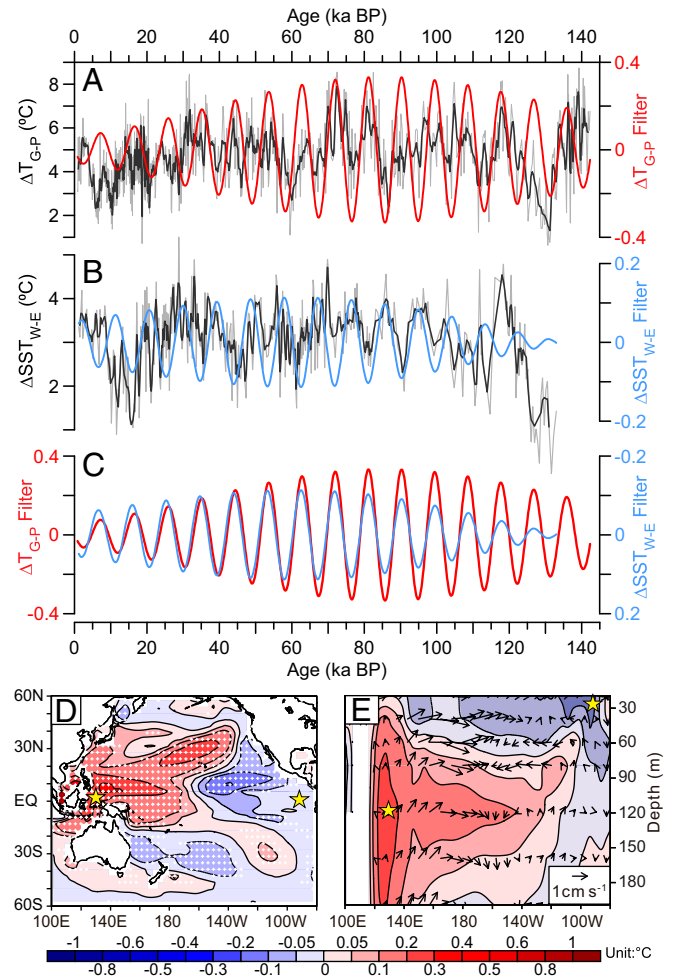


Fig. 5. Link between the upper thermal gradient in the WEP and the west-east SST difference in the equatorial Pacific. (A) ΔT_{G-P} records of core MD01-2386, and (B) the SST difference between the west and east equatorial Pacific (ΔSST_{W-E}) calculated from the SST records of cores MD01-2386 and TR163-22 (17) (detailed in *Methods*). Gray lines are the original records, black thick lines are the five-point moving average filters. Red line in A and blue line in B are band-pass filters at the period of 9.4 ky (frequency = 0.106 ky⁻¹, bandwidth = 0.005); comparison of the band-pass filters is shown in C. Associated half-precessional ENSO-like dynamics in the CESM_{transient} experiment are shown in D and E. (D) Regression coefficients of the annual mean TWT against the half-precessional filter of TWT_{CESM} at site MD01-2386 (red dashed line in *SI Appendix*, Fig. S7B). White dotted areas in D are significant at the 99% confidence level for the ocean temperature. (E) Similar to D but for regression coefficients of the annual mean equatorial ocean temperature (shaded; unit is degrees Celsius) and currents (black arrows indicate horizontal velocity [centimeters per second] and vertical velocity [3.33×10^{-5} cm s⁻¹]) along the latitudes 5°S to 5°N. Yellow stars in D and E show the position of sites MD01-2386 and TR163-22.

TWT, and surface $\delta^{18}\text{O}$ change together during the last termination, but the TWT clearly leads the SST and surface $\delta^{18}\text{O}$ changes during Termination II (Fig. 2). This leading role of the WEP TWT is consistent with modern observations, in which annual mean ocean temperature near the 120-m water depth (rather than at the surface) at site MD01-2386 exhibits the largest anticorrelation with the sea surface temperature in Niño3 region (5°S – 5°N , 150°W – 90°W) (Niño3_SST) (Fig. 1B and C). As an indicator of the warm pool heat content (3), modern WEP TWT has been assumed as an effective precursory ENSO index that triggers El Niño events at the sea surface of the eastern equatorial Pacific (EEP) (59). That means, in the precursory stage of El Niño, a warmer WEP TWT accompanies with a La Niña-like equatorial SST pattern simultaneously (or increased west–east SST gradient; Fig. 1D).

While present-day climate is featured by a strong west–east SST gradient in the equatorial Pacific, paleoclimate records suggest that the mean state of the equatorial Pacific has not always been characterized by such sharp zonal SST gradients due to various timescale fluctuations in the equatorial thermocline (8, 29, 60, 61). The half-precessional signal in TWT should also have its imprint in the surface climate through its impact on the zonal SST gradient along the equator (60, 61), because the WEP thermocline anomaly can regulate the EEP SST through multiple external forcing-modulated air–sea feedbacks (62–64), that is, dynamic movements of thermocline tilt due to an eastward equatorial Kelvin wave (59), or upper oceanic upwelling anomalies in the EEP (64). In order to investigate the orbital-scale behavior of the mean state of the equatorial Pacific, the SST differences between sites MD01-2386 in the WEP and TR163-22 in the EEP (17) are calculated to represent the west–east SST gradient in the equatorial Pacific ($\Delta\text{SST}_{\text{W-E}}$). The age models of both sites are established using the same method and procedure (detailed in *Methods*). As shown in Fig. 5, the $\Delta\text{SST}_{\text{W-E}}$ is well anticorrelated to the $\Delta\text{T}_{\text{G-P}}$ in the WEP at the half-precessional band, with a high cross-spectrum correlation of 0.89, but the amplitude for the $\Delta\text{T}_{\text{G-P}}$ changes is greater, consistent with the “ocean dynamical thermostat” theory (2, 52, 62). Particularly, both $\Delta\text{T}_{\text{G-P}}$ and $\Delta\text{SST}_{\text{W-E}}$ clearly display half-precessional cycles of 9.4 ky, which is not significant in the SST records of either MD01-2386 or TR163-22, reflecting the variability of zonal SST gradient rather than features of any of the original SST time series. It is noted that the half-precessional filter for $\Delta\text{T}_{\text{G-P}}$ at the period of 9.4 ky changes almost simultaneously with the reversal of $\Delta\text{SST}_{\text{W-E}}$ filter (Fig. 5C). This orbital-scale anticorrelation between $\Delta\text{T}_{\text{G-P}}$ and $\Delta\text{SST}_{\text{W-E}}$ is almost the same as that in the modern interannual ENSO pattern, implying that the WEP thermocline water also plays an active role in the past ENSO-like changes over the equatorial Pacific. These half-precessional ENSO-like dynamics are further supported by the CESM_{transient} experiment, in which the TWT at MD01-2386 can represent large parts of the WEP TWT and forms a zonal seesaw with the eastern Pacific upper ocean temperature (Fig. 5D and E), which has been shown earlier as the footprint of the half-precession signal in WEP.

Both modern observation (Fig. 1) and numerical simulation (12, 59) have shown that the upper water thermal structure in the WEP is tightly coupled with an ENSO-like SST anomaly. Therefore, the thermocline temperature change at site MD01-2386 can be used as a sensitive diagnostic tool to track changes in the mean state and its potential modulation of paleo-ENSO variability. Here, the $\Delta\text{T}_{\text{G-P}}$ is well correlated to the surface ENSO-like proxy, $\Delta\text{SST}_{\text{W-E}}$, indicating that the ENSO-like mean state over the equatorial Pacific also has an obvious half-precessional cycle. As discussed above, the TWT and $\Delta\text{T}_{\text{G-P}}$ in the WEP are driven by the meridional insolation gradient in the tropical regimes of both hemispheres, which is related to the precession-paced ENSO-like SST anomaly (63, 64) and the south-

to-north migration of the ITCZ. The half-precessional cycle has been found in records of ITCZ-driven monsoon rainfall at the equator in the Late Quaternary (47) and even in the deep time of the Devonian through Permian (44, 65). This first discovery and understanding of the half-precessional signal in the WEP thermocline builds a bridge to understand long-term changes of ENSO-like variability and ITCZ migration. Untangling the climatic links between the south-to-north migration (monsoon) and the east–west asymmetry (ENSO-like) of the ITCZ through the thermocline temperature change over the Pacific at long timescales will help improve our understanding and projections of future climate change trends in the tropical–extratropical climate.

Methods

Laboratory Measurements. The sediments from core MD01-2386 are olive-gray calcareous ooze with slight bioturbation. The upper 2,088.5 cm of the core was sampled at an average interval of 2 cm. For the stable isotope analyses, about 8 to 12 specimens of *G. ruber sensu stricto* (250 μm to 350 μm) and *P. obliquiloculata* (350 μm to 450 μm) were picked from each sample, while 3 to 10 specimens of benthic *C. wuellerstorfi* (>154 μm) were picked from the samples of 0 cm to 600 cm and 1,680 cm to 1,985 cm in the core. The stable isotope composition was measured by Finnigan-MAT253 mass spectrometer equipped with an automatic carbonate preparation device (Kiel III) at the State Key Laboratory of Marine Geology, Tongji University. The isotopic results were calibrated on the Pee Dee Belemnite scale using the China National standard NBS 19. The SD is $\pm 0.07\%$ for $\delta^{18}\text{O}$ and $\pm 0.05\%$ for $\delta^{13}\text{C}$, respectively.

For the Mg/Ca analyses, foraminiferal specimens were pretreated following the procedure described by Lea et al. (16), but with additional checking and removing of potential contamination performed under a microscope (66), particularly for *P. obliquiloculata*. The Mg/Ca measurements were done using an ICP-MS at the State Key Laboratory of Marine Geology, Tongji University and the Department of Earth Sciences, University of California, Santa Barbara (*SI Appendix, Table S1*). Mn/Ca ratios of *G. ruber* and *P. obliquiloculata* were generally below 0.5 mmol/mol and had no correlation with Mg/Ca, suggesting the Mg/Ca values were not affected by post-depositional Mn-rich oxide or carbonate coatings. Sample reproducibility based on 119 replicates for *G. ruber* and 87 replicates for *P. obliquiloculata* was 2.5% and 4.9%, respectively.

MD01-2386 Age Model. The upper 9.8 m of core MD01-2386 is dated by 17 radiocarbon measurements of *G. ruber* performed in the Leibniz Laboratory of Kiel University (*SI Appendix, Table S2*). The marine reservoir age ΔR is 40 ± 23 y, calculated by the weighted average of eight modern measurements close to the site of core MD01-2386. The top 5 cm of core MD01-2386 appears as a “mudline” (brownish color corresponding to the existence of abundant oxidized particles), but the core-top (0 cm) age is estimated to be 828 y by the linear regression of the ^{14}C dating results over the Holocene interval (0 ka to 10 ka) (*SI Appendix, Fig. S2*). Radiocarbon ages are converted to calendar ages via the calibration curve of Marine13 (67). The depth–age model for the radiocarbon-dated interval is established by the Bayesian statistical methodology of Bacon (68), and the age for 0 cm to 50 cm core depth is linearly interpolated by the estimated core-top age and the age of the first ^{14}C dating point (at 50.5 cm). The settings and results of the Bacon analysis are shown in *SI Appendix, Fig. S2*. The average sedimentation rate is 26.6 cm/ka. Tie-point age model uncertainties derived from Bacon range from 7,351 ± 78 –97 y at 140.5 cm to 36,706 $\pm 1,531$ –1,176 y at 976.5 cm (*SI Appendix, Table S2*).

The depth–age model for the lower part (9.8 m to 21.0 m) of core MD01-2386 is established using the $\delta^{18}\text{O}$ of benthic foraminifer *C. wuellerstorfi* and planktonic foraminifer *G. ruber*. The LR04 benthic $\delta^{18}\text{O}$ stack (24) is utilized as a tuning target for the oxygen isotopic stratigraphic correlation. The establishment of the age model of core MD01-2386 is performed in three steps. Firstly, we compared the benthic $\delta^{18}\text{O}$ record of MD01-2386 with the LR04 benthic stack (*SI Appendix, Fig. S1A*). The two benthic $\delta^{18}\text{O}$ curves are in very good accordance during the period from 20 ka BP to the Late Holocene, the interval where we have plenty of radiocarbon dates. It is inferred that the deep-water $\delta^{18}\text{O}$ variation around site MD01-2386 is generally in phase with the LR04 stack during glacial terminations. Thus, we obtained six age ties to synchronize the benthic $\delta^{18}\text{O}$ of MD01-2386 to LR04 for the penultimate glacial termination (*SI Appendix, Fig. S1A*) from 136 ka BP to 106.5 ka BP.

Then, we compared the *G. ruber* $\delta^{18}\text{O}$ of MD01-2386 with LR04 (*SI Appendix, Fig. S1B*). Using the alignment of *C. wuellerstorfi* $\delta^{18}\text{O}$, the *G. ruber* $\delta^{18}\text{O}$ lags LR04 by about 1 ka to 2 ka during glacial Termination II and the transition from MIS 5e to MIS 5d. For the rest below 9.8 m in the core (between 43.5 ka BP and 91 ka BP, and between 141 ka BP and 154 ka BP), the age ties were obtained by tuning the *G. ruber* $\delta^{18}\text{O}$ to the LR04 stack (*SI Appendix, Fig. S1B and Table S2*). All of the defined age ties of the $\delta^{18}\text{O}$ correlations are shown in *SI Appendix, Table S2*. Finally, the ages between the tie points are given by Bayesian statistical distribution (for ^{14}C dating) or linear interpolation (for $\delta^{18}\text{O}$ -stratigraphic ties) of the most nearby two tie points.

Transient Experiments and the Conceptual Model of Theoretical ΔT . In order to verify the validity of reconstructed ΔT_{G-P} changes, we use CESM with T31_gx3v7 resolution ($3.75^\circ \times 3.75^\circ$ for atmosphere and nominal 3° resolution for ocean) (69) to simulate the SST and TWT at the site of core MD01-2386. As a spin-up, the CESM was first run for 200 model years under orbital parameters and other boundary conditions in AD 1950. Then the model was integrated for 3,000 model years with the transient orbital insolation forcing of the past 300 ky, in which orbital parameters were advanced by 100 y at the end of each model year according to Kutzbach et al. (70). The outputs of this transient experiment (called CESM_{transient} experiment) in the last 3,000 model years were used in our analysis. Comparisons between the simulated and reconstructed ΔT are detailed in *SI Appendix*.

Based on results from this CESM_{transient} experiment and from modern STC studies, here we further presented a conceptual model for the half-precessional changes of ΔT at site MD01-2386. In modern climate, subtropical wind stress forcing and thermal forcing both can affect the WEP TWT through multiple mechanisms (48, 49, 51), including the STC transport volume changes (71, 72), perturbed temperature advections of the mean STC

flow (59, 73), and the fast propagation of oceanic Rossby and Kelvin waves (14, 15, 50). At orbital timescales, we assumed that precessional changes of boreal or austral winter insolation (and associated meridional gradients) will not only induce surface heating anomalies over the STC subduction regions but also modify wind stress conditions from the equator to the extratropics of both hemispheres. Associated STC mechanisms will be simplified as three terms (advection term, volume term, and wave term),

$$\text{Theoretical } \Delta T = \text{Advection} + \text{Volume} + \text{Wave}.$$

Here, the advection term represents the impact of subtropical temperature anomalies (perturbed temperature) on the WEP thermocline through the advection of mean STC flow. The Volume term stands for the impact of STC transport volume changes due to subtropical zonal wind stress anomalies, which are assumed as responses to the equator-to-subtropical insolation gradient during November or May. For the Wave term, we took into consideration the fast response of WEP thermocline depth or temperature through wind-driven oceanic wave pathways of the STC. Detailed calculations are given in *SI Appendix*.

Data Availability. All of the data necessary to assess the validity of this research are presented in the paper and *SI Appendix*.

ACKNOWLEDGMENTS. We thank P. Qiao, X. Cheng, and X. Jiang for providing analytical support, W. Kuhnt for help in the AMS ^{14}C measurements, and anonymous reviewers for their thoughtful reviews. For this research, we used samples provided by the French RV *Marion Dufresne* 122 cruise in 2001. This work was supported by the National Natural Science Foundation of China (Grants 41630965, 91958208, 91428310, 41606045, 41606049, and 41630527), the Ministry of Science and Technology (Grant 2018YFE0202401), the Ministry of Natural Resources of China (Grant GASI-GEOGE-04), and the US NSF P2C2 Program.

- M. A. Cane, M. Evans, CLIMATE VARIABILITY: Enhanced: Do the tropics rule? *Science* **290**, 1107–1108 (2000).
- Z. Liu, B. Huang, A coupled theory of tropical climatology: Warm pool, cold tongue, and Walker circulation. *J. Clim.* **10**, 1662–1679 (1997).
- N. Ramesh, R. Murtugudde, All flavours of El Niño have similar early subsurface origins. *Nat. Clim. Chang.* **3**, 42–46 (2013).
- A. W. Tudhope et al., Variability in the El Niño-Southern Oscillation through a glacial-interglacial cycle. *Science* **291**, 1511–1517 (2001).
- L. Stott, C. Poulsen, S. Lund, R. Thunell, Super ENSO and global climate oscillations at millennial time scales. *Science* **297**, 222–226 (2002).
- K. Xu, R. X. Huang, W. Wang, C. Zhu, R. Lu, Thermocline fluctuations in the equatorial Pacific related to the two types of El Niño events. *J. Clim.* **30**, 6611–6627 (2017).
- M. W. Wara, A. C. Ravelo, M. L. Delaney, Permanent El Niño-like conditions during the Pliocene warm period. *Science* **309**, 758–761 (2005).
- H. L. Ford, A. C. Ravelo, P. S. Dekens, J. P. LaRiviere, M. W. Wara, The evolution of the equatorial thermocline and the early Pliocene *El Padre* mean state. *Geophys. Res. Lett.* **42**, 4878–4887 (2015).
- J. A. Carton, B. S. Giese, A reanalysis of ocean climate using Simple Ocean Data Assimilation (SODA). *Mon. Weather Rev.* **136**, 2999–3017 (2008).
- Z. Liu, S. G. H. Philander, R. Pacanowski, A GCM study of tropical-subtropical upper ocean mass exchange. *J. Phys. Oceanogr.* **24**, 2606–2623 (1994).
- F. A. Schott, W. Wang, D. Stammer, Variability of Pacific subtropical cells in the 50-year ECCO assimilation. *Geophys. Res. Lett.* **34**, L05604 (2007).
- A. Solomon, I. Wainer, Pacific tropical-extratropical thermocline water mass exchanges in the NCAR Coupled Climate System Model v.3. *Ocean Model.* **15**, 218–235 (2006).
- R. X. Huang, Q. Wang, Interior communication window and the structure of the equatorial thermocline. *J. Phys. Oceanogr.* **31**, 3538–3550 (2001).
- L. Wu, Z. Liu, H. E. Hurlburt, Kelvin wave and Rossby wave interaction in the extratropical-tropical Pacific. *Geophys. Res. Lett.* **27**, 1259–1262 (2000).
- Z. Liu, L. Wu, E. Bayler, Rossby wave-Coastal Kelvin wave interaction in the extratropics, Part I: Low-frequency adjustment in a closed basin. *J. Phys. Oceanogr.* **29**, 2382–2404 (1999).
- D. W. Lea, D. K. Pak, H. J. Spero, Climate impact of late quaternary equatorial Pacific sea surface temperature variations. *Science* **289**, 1719–1724 (2000).
- D. W. Lea et al., Paleoclimate history of Galápagos surface waters over the last 135,000 yr. *Quat. Sci. Rev.* **25**, 1152–1167 (2006).
- M. Hollstein et al., Stable oxygen isotopes and Mg/Ca in planktic foraminifera from modern surface sediments of the western Pacific warm pool: Implications for thermocline reconstructions. *Paleoceanography* **32**, 1174–1194 (2017).
- P. Anand, H. Elderfield, M. H. Conte, Calibration of Mg/Ca thermometry in planktonic foraminifera from a sediment trap time series. *Paleoceanography* **18**, 1050 (2003).
- C. Cléroux et al., Mg/Ca and Sr/Ca ratios in planktonic foraminifera: Proxies for upper water column temperature reconstruction. *Paleoceanography* **23**, PA3214 (2008).
- H. Dang et al., The calcification depth and Mg/Ca thermometry of *Pulleniatina obliquiloculata* in the tropical Indo-Pacific: A core-top study. *Mar. Micropaleontol.* **145**, 28–40 (2018).
- M. Mohtadi et al., North Atlantic forcing of tropical Indian Ocean climate. *Nature* **509**, 76–80 (2014).
- U. Pflaumann, Z. Jian, Modern distribution patterns of planktonic foraminifera in the South China Sea and western Pacific: A new transfer technique to estimate regional sea-surface temperatures. *Mar. Geol.* **156**, 41–83 (1999).
- L. E. Lisiecki, M. E. Raymo, A Pliocene-Pleistocene stack of 57 globally distributed benthic $\delta^{18}\text{O}$ records. *Paleoceanography* **20**, PA1003 (2005).
- M. Blaauw, J. A. Christen, K. D. Bennett, P. J. Reimer, Double the dates and go for Bayes—Impacts of model choice, dating density and quality on chronologies. *Quat. Sci. Rev.* **188**, 58–66 (2018).
- J. Xu, A. Holbourn, W. Kuhnt, Z. Jian, H. Kawamura, Changes in the thermocline structure of the Indonesian outflow during Terminations I and II. *Earth Planet. Sci. Lett.* **273**, 152–162 (2008).
- J. Ahn, E. J. Brook, Atmospheric CO_2 and climate on millennial time scales during the last glacial period. *Science* **322**, 83–85 (2008).
- T. Blunier, E. J. Brook, Timing of millennial-scale climate change in Antarctica and Greenland during the last glacial period. *Science* **291**, 109–112 (2001).
- L. D. Pena, I. Cacho, P. Ferretti, M. A. Hall, El Niño-Southern Oscillation-like variability during glacial terminations and interlatitudinal teleconnections. *Paleoceanography* **23**, PA3101 (2008).
- L. Lo et al., Nonlinear climatic sensitivity to greenhouse gases over past 4 glacial/interglacial cycles. *Sci. Rep.* **7**, 4626 (2017).
- J. D. Shakun et al., Global warming preceded by increasing carbon dioxide concentrations during the last deglaciation. *Nature* **484**, 49–54 (2012).
- R. Saraswath, D. W. Lea, R. Nigam, A. Mackensen, D. K. Naik, Deglaciation in the tropical ocean driven by interplay between the regional monsoon and global teleconnections. *Earth Planet. Sci. Lett.* **375**, 166–175 (2013).
- S. A. Marcott et al., Centennial-scale changes in the global carbon cycle during the last deglaciation. *Nature* **514**, 616–619 (2014).
- M. Hollstein et al., Variations in Western Pacific Warm Pool surface and thermocline conditions over the past 110,000 years: Forcing mechanisms and implications for the glacial Walker circulation. *Quat. Sci. Rev.* **201**, 429–445 (2018).
- M. Schulz, M. Mudelsee, REDFIT: estimating red-noise spectra directly from unevenly spaced paleoclimatic time series. *Comput. Geosci.* **28**, 421–426 (2002).
- K. B. Orlafsdottir, M. Schulz, M. Mudelsee, REDFIT-X: Cross-spectral analysis of unevenly spaced paleoclimate time series. *Comput. Geosci.* **91**, 11–18 (2016).
- F. Regoli et al., Progressive shoaling of the equatorial Pacific thermocline over the last eight glacial periods. *Paleoceanography* **30**, 439–455 (2015).
- A. Berger, M. F. Loutre, Intertropical latitudes and precessional and half-precessional cycles. *Science* **278**, 1476–1478 (1997).
- M. Regenberg, A. Regenberg, D. Garbe-Schonberg, D. W. Lea, Global dissolution effects on planktonic foraminiferal Mg/Ca ratios controlled by the calcite-saturation state of bottom waters. *Paleoceanography* **29**, 127–142 (2014).
- B. L. Rongstad, T. M. Marchitto, J. C. Herguera, Understanding the effects of dissolution on the Mg/Ca paleothermometer in planktonic foraminifera: Evidence from a novel individual foraminifera method. *Paleoceanography* **32**, 1386–1402 (2017).
- J. Le, N. J. Shackleton, Carbonate dissolution fluctuations in the western equatorial Pacific during the Late Quaternary. *Paleoceanography* **7**, 21–42 (1992).
- Z. Jian, B. Huang, H. Lin, W. Kuhnt, Late quaternary upwelling intensity and East Asian monsoon forcing in the South China Sea. *Quat. Res.* **55**, 363–370 (2001).

43. M. Mohtadi *et al.*, Low-latitude control on seasonal and interannual changes in planktonic foraminiferal flux and shell geochemistry off south Java: A sediment trap study. *Paleoceanography* **24**, PA1201 (2009).
44. R. Y. Anderson, Enhanced climate variability in the tropics: A 200 000 yr annual record of monsoon variability from Pangea's equator. *Clim. Past* **7**, 757–770 (2011).
45. D. A. Short, J. G. Mengel, T. J. Crowley, W. T. Hyde, G. R. North, Filtering of Milankovitch cycles by earth's geography. *Quat. Res.* **35**, 157–173 (1991).
46. A. McIntyre, B. Molino, Forcing of Atlantic equatorial and subpolar millennial cycles by precession. *Science* **274**, 1867–1870 (1996).
47. D. Verschuren *et al.*; CHALLACEA project members, Half-precessional dynamics of monsoon rainfall near the East African equator. *Nature* **462**, 637–641 (2009).
48. S. Shin, Z. Liu, Response of the equatorial thermocline to extratropical buoyancy forcing. *J. Phys. Oceanogr.* **30**, 2883–2905 (2000).
49. L. Hong, L. Zhang, Z. Chen, L. Wu, Linkage between the Pacific Decadal Oscillation and the low frequency variability of the Pacific Subtropical Cell. *J. Geophys. Res. Oceans* **119**, 3464–3477 (2014).
50. Z. Liu, Forced planetary wave response in a thermocline gyre. *J. Phys. Oceanogr.* **29**, 1036–1055 (1999).
51. H. Yang, Z. Liu, H. Wang, Influence of extratropical thermal and wind forcings on equatorial thermocline in an ocean GCM. *J. Phys. Oceanogr.* **34**, 174–187 (2004).
52. G. Graffino, R. Farneti, F. Kucharski, F. Molteni, The effect of wind stress anomalies and locations in driving Pacific subtropical cells and tropical climate. *J. Clim.* **32**, 1641–1660 (2019).
53. Z. Liu, J. Kutzbach, L. Wu, Modeling climatic shift of El Niño variability in the Holocene. *Geophys. Res. Lett.* **27**, 2265–2268 (2000).
54. P. Lu, J. P. McCreary, Influence of the ITCZ on the flow of the thermocline water from the subtropical to the equatorial Pacific Ocean. *J. Phys. Oceanogr.* **25**, 3076–3088 (1995).
55. M. W. Wara, A. C. Ravelo, J. S. Revenaugh, The pacemaker always rings twice. *Paleoceanography* **15**, 616–624 (2000).
56. P. Ferretti, S. J. Crowhurst, M. A. Hall, I. Cacho, North Atlantic millennial-scale climate variability 910 to 790 ka and the role of the equatorial insolation forcing. *Earth Planet. Sci. Lett.* **293**, 28–41 (2010).
57. K. Visser, R. Thunell, L. Stott, Magnitude and timing of temperature change in the Indo-Pacific warm pool during deglaciation. *Nature* **421**, 152–155 (2003).
58. D. W. Lea, The 100,000-yr cycle in tropical SST, greenhouse forcing, and climate sensitivity. *J. Clim.* **17**, 2170–2179 (2004).
59. B. T. Anderson, R. C. Perez, A. Karspeck, Triggering of El Niño onset through trade wind-induced charging of the equatorial Pacific. *Geophys. Res. Lett.* **40**, 1212–1216 (2013).
60. A. V. Fedorov, N. J. Burls, K. T. Lawrence, L. C. Peterson, Tightly linked zonal and meridional sea surface temperature gradients over the past five million years. *Nat. Geosci.* **8**, 975–980 (2015).
61. A. V. Fedorov *et al.*, Patterns and mechanisms of early Pliocene warmth. *Nature* **496**, 43–49 (2013).
62. Y. Luo, J. Lu, F. Lu, O. Garuba, The role of ocean dynamical thermostat in delaying the El Niño-like response over the equatorial Pacific to climate warming. *J. Clim.* **30**, 2811–2817 (2017).
63. A. Timmermann, S. J. Lorenz, S.-I. An, A. Clement, S.-P. Xie, The effect of orbital forcing on the mean climate and variability of the tropical Pacific. *J. Clim.* **20**, 4147–4159 (2007).
64. Z. Liu *et al.*, Evolution and forcing mechanisms of El Niño over the past 21,000 years. *Nature* **515**, 550–553 (2014).
65. D. De Vleeschouwer, A. C. Da Silva, F. Boulvain, M. Crucifix, P. Claeys, Precessional and half-precessional climate forcing of Mid-Devonian monsoon-like dynamics. *Clim. Past* **8**, 337–351 (2012).
66. S. Barker, M. Greaves, H. Elderfield, A study of cleaning procedures used for foraminiferal Mg/Ca paleothermometry. *Geochem. Geophys. Geosyst.* **4**, 8407 (2003).
67. M. Stuiver, P. J. Reimer, R. W. Reimer, (2018) CALIB 7.1 [WWW program]. <http://calib.org>. Accessed 27 July 2018.
68. M. Blaauw, J. A. Christen, Flexible paleoclimate age-depth models using an autoregressive gamma process. *Bayesian Anal.* **3**, 457–474 (2011).
69. C. A. Shields *et al.*, The low-resolution CCSM4. *J. Clim.* **25**, 3993–4014 (2012).
70. J. E. Kutzbach, X. D. Liu, Z. Y. Liu, G. S. Chen, Simulation of the evolutionary response of global summer monsoons to orbital forcing over the past 280,000 years. *Clim. Dyn.* **30**, 567–579 (2008).
71. R. Kleeman, J. P. McCreary Jr, B. A. Klinger, A mechanism for generating ENSO decadal variability. *Geophys. Res. Lett.* **26**, 1743–1746 (1999).
72. M. J. McPhaden, D. Zhang, Slowdown of the meridional overturning circulation in the upper Pacific Ocean. *Nature* **415**, 603–608 (2002).
73. D. Gu, S. G. H. Philander, Interdecadal climate fluctuations that depend on exchanges between the tropics and extratropics. *Science* **275**, 805–807 (1997).